Electrochimica Acta 272 (2018) 144–153

Contents lists available at ScienceDirect

Electrochimica Acta

journal homepage: www.elsevier.com/locate/electacta

Processing liquid-feed flame spray pyrolysis synthesized $Mg_{0.5}Ce_{0.2}Zr_{1.8}(PO_4)_3$ nanopowders to free standing thin films and pellets as potential electrolytes in all-solid-state Mg batteries

B. Liang [a, b], V. Keshishian [a], S. Liu [a, b], E. Yi [a], D. Jia [b], Y. Zhou [b], J. Kieffer [a], B. Ye [c], R.M. Laine [a, *]

[a] Dept. of Mater. Sci. and Eng., University of Michigan, Ann Arbor, MI 48109-2136, USA
[b] Institute for Advanced Ceramics, School of Mater. Sci. and Eng., Harbin Institute of Tech., Harbin, 150080, China
[c] National Engineering Research Center of Light Alloy Net Forming and State Key Laboratory of Metal Matrix Composites, Shanghai Jiao Tong University, Shanghai, 200240, China

ARTICLE INFO

Article history:
Received 27 November 2017
Received in revised form
28 March 2018
Accepted 2 April 2018
Available online 4 April 2018

Keywords:
LF-FSP
Nanopowders
Thin films
Solid magnesium electrolyte
Magnesium ion battery

ABSTRACT

Despite the intense concentration on lithium-based batteries, safety, ease of construction and cost continue to drive the search for alternatives that do not suffer from such restrictions. We present here preliminary work on the development of thin film Mg^{2+} conducting electrolytes as the key starting point for the development of all-solid-state Mg batteries. Initial studies explored compositions in the $Mg_{0.5}Ce_xZr_{2-x}(PO_4)_3$ (x = 0.1, 0.2 and 0.3) system first as pellets and with somewhat optimized compositions (with x = 0.2) as thin films. Introduction of Ce allows sintering to full density at temperatures where Ce free films do not densify completely. The work reported here relies on the synthesis of nanopowders (NPs) using liquid-feed flame spray pyrolysis that offers the potential to reduce processing conditions, to control final average grain sizes (AGSs) and provide single-phase materials with good to excellent mechanical properties. The pellets and then thin (≤50 μm) films produced here show conductivities of up to 3×10^{-3} mS cm^{-1} at ≈ 300 °C, which if extrapolated (using an E_a of ≈30) to 400 °C would be close to 10^{-2} mS cm^{-1} in keeping with the best reported values in the literature. The thin films reported here offer nearly full densities beyond what is currently achievable by any other method. The ionic area specific resistance (IASR) values for these thin films were found to be 1400 Ω cm^2 at 300 °C and are estimated to drop to 110 Ω cm^2 at 400 °C, significantly lower than values for pellets reported elsewhere.

1. Introduction

Electrical energy storage demands of electric devices (including electric vehicles, laptop computers, load leveling for stationary power sources and cellular phones for example), coupled with fossil fuel economies and limitations demonstrate the growing need for rechargeable batteries with multiple performance capabilities including sufficient energy density, appropriate voltage and current capabilities, and perhaps most important very low safety requirements. Conventional liquid electrolytes lithium batteries suffer from the potential to fail catastrophically via electrolyte leakage, boiling, freezing, combustion or even explosion, of particular importance for in vivo applications [1–3]. There is need to develop batteries with much higher safety and greater energy densities to satisfy growing market demands. Under such circumstances, all-solid-state batteries (ASBs) have been proposed as a fundamental solution [4]. They do not require liquid electrolytes relieving this avenue for catastrophic failure. They are also capable of operating over wide temperature and electrochemical potential ranges. Coincidently, metal anodes and high-voltage cathodes can be used to greatly enhance energy densities allowing long term operation without need to recharge. Likewise, the potential for much greater operating temperature ranges implies faster charge/discharge properties.

To date, the most successful and widely implemented rechargeable battery technologies rely on lithium. Efforts to

* Corresponding author.
E-mail address: talsdad@umich.edu (R.M. Laine).

https://doi.org/10.1016/j.electacta.2018.04.015
0013-4686/

develop rechargeable Li ASBs have attracted much attention due to their high voltage and high theoretical energy density of 3500 Wh·kg^{-1}, and can, when perfected, play a pivotal role as an advanced electrochemical power source [3,5,6]. However, the low accessibility of Li (e.g. low natural abundance of 7 g/F in the earth's crust and 0.04–1.16% in brine ponds) goes against its sustainability. High and probably rising costs also limit the future use of Li^+ batteries for large-scale applications [6–8].

Given the need for a sustainable supply of large-scale energy storage devices, considerable efforts have been directed towards the development of non-lithium battery systems, especially ASBs. Of the possible alternatives, rechargeable magnesium-ion (Mg^{2+}) battery technology offers significant opportunities for the following reasons. First is Mg's high natural abundance in the earth's crust (5th most abundant element, approximately 10^4 times that of Li), allowing low-cost incorporation into battery elements. Second, the divalent nature of Mg ions also allows a high volumetric capacity of 3833 mAh/cc (vs. 2046 mAh/cc for lithium). Third, Mg provides a higher atmospheric stability and melting point than Li making it safer compared to Li. Mg also has a rather low equivalent weight of 12 g per Faraday (F) (vs. 7 g/F for Li, 23 g/F for Na) and low price of ca $2700/ton (currently ca. 24 times cheaper than Li) ensuring a feasible, "environmentally-friendly" alternative to the immensely popular Li-ion systems [6,8–21].

To date, there have been a number of reviews [7–10] discussing the potential offered by Mg based batteries. Much of the literature on Mg based batteries that function near ambient focuses on the use of liquid electrolytes [18–21]. Thus, the same issues of safety would apply for any system that was commercialized. Despite the exceptional interest in making solid state Mg electrolytes [1,7–9,15–17,22], only one recent theoretical paper suggests that it should be possible to make solid state electrolytes with near ambient conductivities sufficient to be used to generate solid state Mg based batteries [14]. Thus, at present Mg based solid state batteries seem to offer potential only for high temperature applications.

Despite these positive attributes, the development of Mg-based ASBs has not kept pace with Li batteries. One critical issue impeding progress is the availability of stable and highly Mg^{2+}-conducting solid electrolytes that enable reversible release of Mg^{2+} ions from a magnesium metal anode. To date, there exist only limited reports on Mg^{2+}-conducting solid electrolytes. $Mg_{0.5}Zr_2(PO_4)_3$, MZP, is well-known among them to have a 3-D network linking ZrO_6 octahedra and PO_4 tetrahedra by corner-sharing [18–21]. MZP has two crystal morphologies. The β-$Fe_2(SO_4)_3$-type MZP (monoclinic symmetry, $P2_1/n$ space group) would offer reduced conductivities at low temperatures due to the distortion of the β-$Fe_2(SO_4)_3$ structure. MZP can also offer a NASICON (Na^+ super ionic conductor) structure (rhombohedral symmetry with hexagonal setting, *R*3*c*) where well-ordered $Zr_2P_3O_{12}$ (lantern) units allow smooth ion migration. Therefore, high ion conductivity is expected at moderate temperatures (300°-500 °C) due to the low activation energy for ion migration.

Of the available reports on MZP systems, pellet-shaped electrolytes have been explored by a number of groups synthesized mainly using solid-state synthetic [21–24] and sol-gel methods [15–17]. Ikeda et al. [21,22,26] first investigated solid MZP electrolytes to develop potentiometric sensors. As-processed MZP pellets exhibited the expected $Na_{0.5}Zr_2(PO_4)_3$ structure with conductivities ranging from 2.9×10^{-2} mS cm^{-1} (400 °C) to 6.1 mS cm^{-1} (800 °C) and activation energies of ≈80 kJ/mol [21].

Imanaka et al. [23] also prepared MZP pellets by solid state processing finding Mg^{2+} conductivities were considerably enhanced predominantly due to the microscopic dispersion of a $Zr_2O(PO_4)_2$ secondary phase in the composite. Additionally, Anuar et al. [15,16] prepared MZP pellets with a pure NASICON-phase by sol-gel processing observing conductivities of 1.0×10^{-3} mS cm^{-1} at ambient and 7.1×10^{-2} mS cm^{-1} at 500 °C with electrochemical stabilities up to 2.50 V vs a Mg/Mg^{2+} electrode. Adamu et al. [17] reported a conductivity of 6.9 mS cm^{-1} at 800 °C for dense (ca. 99 % TD), single-phase MZP pellets produced using a novel sol-gel approach.

Efforts to improve the performance of MZP compounds have targeted modification of the lattice structures [16,27–29]. Thus substitution of Fe^{3+} (0.65 Å ionic radius) for Zr^{4+} (0.72 Å) is expected to reduce lattice dimensions providing more suitable channel sizes for Mg^{2+} (0.72 Å) migration. It also introduces extra interstitial Mg^{2+} ions in the NASICON structure anticipated to enhance the concentration of available Mg^{2+} ions [28]. Thus, introduction of Fe^{3+} increases charge carrier concentrations and mobile ion concentrations. The partially Fe-substituted MZP, i.e. $Mg_{0.9}(Zr_{0.6}Fe_{0.4})_2(PO_4)_3$ gives a maximum conductivity of 1.3×10^{-2} mS cm^{-1} at room temperature and 7.2×10^{-2} mS cm^{-1} at 500 °C, an order of magnitude higher than that of the parent MZP compound [16].

The thicknesses (1–2 mm) of pellet components including electrodes and electrolytes limit gravimetric/volumetric energy densities of assembled cells. Thicker components with relatively higher internal resistance cause lower power output (poor rate capability) and an earlier stop of discharge (particularly high rate discharge) due to longer diffusion distances and severe concentration polarization [30–33]. Compared to pellets, thin (≤100 μm) film electrolytes are therefore more competitive and useful in assembling cells with high packing densities and structural stability ensuring high safety and overall performance of assembled battery systems [34–43]. One can envision developing solid-state batteries with superior energy densities through significant reductions in the electrolytes and electrode thicknesses opening a new door for Mg batteries.

We recently described methods of processing dense $Li_{1.7}Al_{0.3}Ti_{1.7}Si_{0.4}P_{2.6}O_{12}$ pellets with ambient ionic conductivities >1 mS cm^{-1} [37]. Significantly, we also learned to process dense, flexible Li^+-conducting ceramic electrolyte thin films (≤50 μm) using tape-casting methods based on liquid-feed flame spray pyrolysis (LF-FSP) nanopowders (NPs). These systems provide high ambient ionic conductivities (e.g. 0.4 mS cm^{-1} for 50 μm $Li_{1.7}Al_{0.3}Ti_{1.7}Si_{0.4}P_{2.6}O_{12}$ [37], 0.2 mS cm^{-1} for 30 μm c-$Li_7La_3Zr_2O_{12}$ [38], 1.3 mS cm^{-1} for 25 μm Ga:LLZO [39]) and high tolerance to heat improving safety over wide operating temperatures.

In this contribution, we extend our efforts to develop Ce-doped MZP thin film electrolytes with chemical compositions near $Mg_{0.5}Ce_xZr_{2-x}(PO_4)_3$ (x = 0.1, 0.2 and 0.3), hereinafter referred to as $MZPCe_x$. Ce^{4+} (0.87 Å) is expected to substitute for Zr^{4+} (0.72 Å) as an alternative to Fe^{3+} to improve MZP conductivities. $MZPCe_x$ pellets ($\Phi 12 \times 0.5$ mm^2) were first studied to optimize compositions, and then thin (≤50 μm) films were processed with these somewhat optimized compositions. Pellets and thin films with compositions of $Mg_{0.5}Ce_{0.2}Zr_{1.8}(PO_4)_3$ offer ionic conductivities in keeping with the best reported values in the literature [15,17,20,23].

2. Experimental

2.1. Raw materials

Magnesium hydroxide [$Mg(OH)_2$], propionic acid (CH_3CH_2COOH), isobutyric acid [$(CH_3)_2CHCO_2H$], isobutyric anhydride [$(C_3H_7CO)_2O$], zirconium basic carbonate, [$Zr(OH)_2CO_3 \cdot ZrO_2$], triethyl phosphate [$(C_2H_5O)_3PO$], cerium carbonate [$Ce_2(CO_3)_3 \cdot xH_2O$], methyl ethyl ketone ($C_2H_5COCH_3$) and benzyl butylphthalate {2-[$CH_3(CH_2)_3O_2C]C_6H_4CO_2CH_2C_6H_5$, 98%} were

purchased from Sigma-Aldrich (Milwaukee, WI). Polyvinyl butyral [$(C_8H_{14}O_2)_n$, B-98, $M_n = 40{,}000–70{,}000$] was purchased from Butvar (Avon, OH), and absolute ethanol from Decon Labs (King of Prussia, PA).

2.2. Precursor synthesis

As-purchased triethyl phosphate, $(C_2H_5)_3PO_4$, was directly used as the P source. The other three precursors were synthesized as sources of Mg, Zr, and Ce, respectively as follows.

Magnesium propionate, $Mg(O_2CCH_2CH_3)_2$, was synthesized by reacting $Mg(OH)_2$ (157 g, 2.7 mol) with excess $CH_3CH_2CO_2H$ (500 ml, 6.8 mol) in a 1 L round-bottom flask equipped with a still head. The mixture was heated at 130 °C for 2 h with magnetic stirring until it became transparent. On cooling to room temperature, magnesium propionate crystallized, then was filtered off, dried naturally, ground into powder for use. As-obtained Mg precursor provided a ceramic yield of ca. 42 wt %, lower than theoretical value (44 wt %), as determined by TGA. The discrepancy arises mainly from slight excess of propionic acid.

Zirconium isobutyrate, $Zr[O_2CCH(CH_3)_2]_2(OH)_2$, was synthesized by reacting zirconium basic carbonate (160 g, 0.52 mol) with isobutyric acid (390 g, 4.4 mol) and isobutyric anhydride (350 g, 2.2 mol) in a 1 L flask equipped with a still head in N_2 atmosphere. The reactants were heated at 110 °C until they became transparent. Zirconium isobutyrate crystallized on cooling, then was filtered off, dried, ground into powder for use.

Cerium propionate [$Ce(O_2CCH_2CH_3)_3(OH)$] was synthesized by reacting cerium carbonate (46 g, 0.1 mol) with excess propionic acid (225 mL, 3 mol) and propionic anhydride (65 mL, 0.5 mol) in a 1 L flask equipped with a still head. The solution was heated at 120 °C for 10 h with magnetic stirring until a transparent dark orange liquid was obtained. On cooling to room temperature, cerium propionate crystallized and was filtered out.

2.3. Nanopowder (NP) syntheses

$Mg_{0.5}Ce_xZr_{2-x}(PO_4)_3$ (x = 0.1, 0.2 and 0.3) NPs were synthesized by liquid feed-flame spray pyrolysis (LF-FSP) technology described in detail elsewhere [40–43]. All the precursors for Mg, Zr, P, Ce were mixed and dissolved in ethanol at designated ratios providing a solution with 3 wt % ceramic yield. The as-formulated precursor solution was aerosolized with oxygen into a 1.5 m long combustion chamber and ignited using methane/O_2 pilot torches. After combustion and cooling, NPs were collected downstream in wire-in-tube electrostatic precipitators operated at 10 kV, then cleaned by dispersing them into EtOH using an ultrasonic horn (Vibra-cell VC-505, Sonics & Mater. Inc.). After sufficient sedimentation, the supernatant suspension was decanted into a container, dried in an oven and collected for use.

2.4. Pellet processing

The dried $MZPCe_x$ powders were sieved through a 20 μm polymer mesh, uniaxially pressed at 12 MPa in a biaxial-compression WC die (14.2 mm in diam.), and CIPped at 200 MPa for 30 min improving densities of green bodies. Green pellets were sintered in air at 1100–1200 °C for 1 h with a ramp rate of 5 °C/min.

2.5. Thin film processing

As-synthesized $MZPCe_{0.2}$ NPs were mixed with binder, plasticizer and solvents with designated ratios (as listed in Table 1), then ball-milled for 24 h with zirconia beads (99% in purity, 3.0 mm in diam.) homogenizing the suspension.

Table 1
Starting chemical components for film casting.

Components	Roles	Mass (g)	Wt.%	Vol%
$MZPCe_{0.2}$	Powder	1.00	32	10
Polyvinyl butyral (PVB)	Binder	0.13	4	4
Benzyl butyl phthalate (BBP)	Plasticizer	0.13	4	4
Methyl ethyl ketone (MEK)	Solvent	0.95	30	41
Ethanol	Solvent	0.95	30	41

The suspension was cast using a wire-wound rod coater (Automatic Film Applicator-1137, Sheen Instrument, Ltd., UK) producing thin NP filled polymeric films. Film thicknesses were controlled using spacers between the rod and Mylar substrate. After solvent evaporation, dried green films were cut into small pieces, uniaxially pressed at 30 MPa/100 °C/3 min using a heated bench-top press (Carver, Inc), then manually peeled off the substrate.

Dried, green $MZPCe_{0.2}$ films were debindered/crystallized in air at 785 °C/1 h heating at a ramp rate of 5 °C/min followed by sintering at 1000–1200 °C for selected dwell times. During heating, films were placed between α-alumina plates to prevent warping.

2.6. Thermal etching of as-sintered films

To calculate average grain sizes using the lineal intercept method, as-sintered films were thermally etched to expose separate grains by heating in air for 30 min at designated temperatures for 30 min in air. The temperatures of thermal etching were usually 100 °C lower than sintering temperatures of films.

2.7. Characterization

Specific surface area (SSA) analyses of the as-shot $MZPCe_{0.2}$ NPs were obtained using a Micromeritics ASAP 2010 N_2 adsorption analyzer (Norcross, GA). Samples (ca. 200 mg) were degassed at 400 °C until the degas rate was less than 0.005 Torr/min, then analyzed at −196 °C (77 K) in N_2. SSAs were calculated using the BET multipoint (≥10 points) method within the relative pressure range of 0.001–0.20. Additionally, the average particle sizes (APSs), D, can be calculated per formula [44]:

$$D = 2r = 6/(\rho \times SSA)$$

where ρ is the theoretical density of powders, and r is the particle radius.

2.7.1. Thermogravimetric/differential scanning calorimetry (TG/DTA)

Thermal decomposition and crystallization of as-cast green films were analyzed using Q600 simultaneous TG/DTA (TA Instruments, Inc.) predicting the progress of film thermal behavior. Samples (ca. 15 mg) were loaded in an alumina pan, heated from ambient temperature to 1200 °C with a ramp rate of 10 °C/min in a flowing synthetic air (60 mL/min).

X-ray diffraction (XRD) (Rigaku Denki., LTD., Tokyo, Japan) was conducted at 40 kV and 100 mA for phase identification of LF-FSP NPs and sintered films and pellets. Note that the pellets were broken up, ground into powders and then characterized by XRD. Samples were scanned by Cu Kα radiation (λ = 1.541 Å) at 2°/min within the range of 10–70° 2θ with 0.02° intervals. Jade 2010 software (Version 1.1.5 from Mater. Data, Inc.) was used to analyze XRD data where JCPDS files were used including $Mg_{0.5}Zr_2(PO_4)_3$ (04-016-0487), ZrP_2O_7 (04-009-9317) and ZrO_2 (98-000-9216). The Jade software (2010, Version 1.1.5 from Materials Data, Inc.,

Livermore CA) was used to refine lattice constants, and to determine the presence of crystallographic phases calculating their relative contents.

Scanning electron microscopy (SEM) (NOVA Nanolab, FEI Inc.) was run at 20 kV and used to observe powder and film morphologies. All the samples were sputter coated with a gold film using a Technics Hummer VI sputtering system (Anatech Ltd., Alexandria, VA) to improve resolution.

Transmission Electron Microscopy (TEM) (JEOL 3011) was conducted at 300 kV to study film microstructures including grain sizes and phases. As-sintered 40 μm thick films were cut to 3 mm in diam., gently polished, dimpled, and Ar-ion thinned to perforation.

Ionic conductivity measurements were run using an AC broadband dielectric impedance spectrometer (Novocontrol technologies, Hundsangen, Germany) to evaluate the ionic conductivity of as-sintered $MZPCe_{0.2}$ films. All film surfaces were gently polished using 1200 grit SiC sandpapers (LECO, St. Joseph, MI), then coated with gold coatings using an SPI sputter coater (SPI Supplies Inc., West Chester, PA). Gold electrode with a diam. of 1 mm was deposited on one side of film surface, while the other side was coated in full. Ionic conductivity measurements were operated at 60–280 °C with a frequency range of 10 MHZ to 0.1 HZ and a root mean square (RMS) voltage of 10 mV.

Nyquist plots were fitted using EIS spectrum analyzer software to get total resistance of samples [45]. Conductivities (σ_t) were calculated from formula [46,47].

$$\sigma_t = d/(A_e \times R) \quad (1)$$

where d, A_e, R denote film thickness, electrode area and total resistance, respectively.

Activation energies, E_a, were calculated from Arrhenius equation [15,48].

$$\sigma_t = A\exp(-E_a/R_gT) \quad (2)$$

where A, R_g, T mean pre-exponential factor, gas constant and absolute temperature, respectively.

3. Results and discussion

3.1. As-produced NPs

As seen in Fig. 1a SEM, as-produced $MZPCe_{0.2}$ NPs typical of MZP_x (x = 0.1, 0.2 and 0.3) consist of spherical agglomerated particles with few obvious aggregates. Most of the powders exhibit average particle sizes (APSs) < 100 nm with no micron sized particles. BET studies indicate SSAs of 28 m^2/g allowing calculation of APSs of ca. 66 nm, in accord with SEM results.

Fig. 1b XRD indicates these NPs consist primarily of MZP (74 wt %) with the remaining phases being ZrP_2O_7 (9 wt %) and ZrO_2 (17 wt %). The broad XRD peaks are typical of nanoscale particles. It should be noted that the presence of some partially amorphous powders cannot be excluded.

3.2. Thermal analysis of green films

As-cast green films were heated to 1200 °C/air with a ramp rate of 10 °C/min as a prelude to extensive further studies on sintering films and pellets. Thermal analysis (Fig. S1) shows continuous, significant mass losses (until around 550 °C) accompanied by exotherms arising at 320° and 500 °C, due mainly to decomposition of polymer additives, see Table 1. Mass losses cease at 550–600 °C corresponding to a ceramic yield of 79 wt % almost identical to theory derived from Table 1. The expected ceramic yields of processed green films can be calculated as 80 wt % (56 vol %), excluding solvents (MEK and ethanol) as they would evaporate on drying. The exotherm at 783 °C is likely associated with the crystallization of MZP and ZrP_2O_7 phases [15]. The endotherm seen above 1120 °C, accompanied by a slight mass loss, is most likely due to the evaporation of PO_x species [17,23].

3.3. MZPCe$_x$ pellets

Fig. 2 provides XRDs for $MZPCe_x$ (x = 0.1, 0.2 and 0.3) pellets after sintering at 1200 °C/1 h/air. The as-sintered pellets consist mainly of $Mg_{0.5}Zr_2(PO_4)_3$ and ZrP_2O_7 phases. As reported elsewhere, zirconium phosphate including $Zr_2P_2O_9$ and ZrP_2O_7 are typical impurities detected in MZP materials [17,25]. $MZPCe_{0.1}$ pellets offer ca. 97 wt % MZP, while for most $MZPCe_{0.2}$ and $MZPCe_{0.3}$ pellets phase purity is closer to 90 wt % (Table 2).

Fig. 3 SEMs indicate that sintering $MZPCe_x$ at 1200 °C/1 h/air offers almost fully dense $MZPCe_{0.2}$ and $MZPCe_{0.3}$ pellets, but porous $MZPCe_{0.1}$ pellets with a relative density of ≈90% (Table 2).

Note that the $MZPCe_{0.2}$ pellets were also sintered at 1100 °C/1 h, 1200 °C/3 h, respectively. Unfortunately, lower temperatures lead to porous structures, and longer dwell times at 1200 °C lead to lower MZP phase contents. Higher temperatures and longer dwell times probably cause PO_x loss (SEM and EDS not shown), which leads to lower phase purities. *Ce-free MZP samples do not densify on sintering at 1000–1200 °C under the same conditions* (SEM not shown).

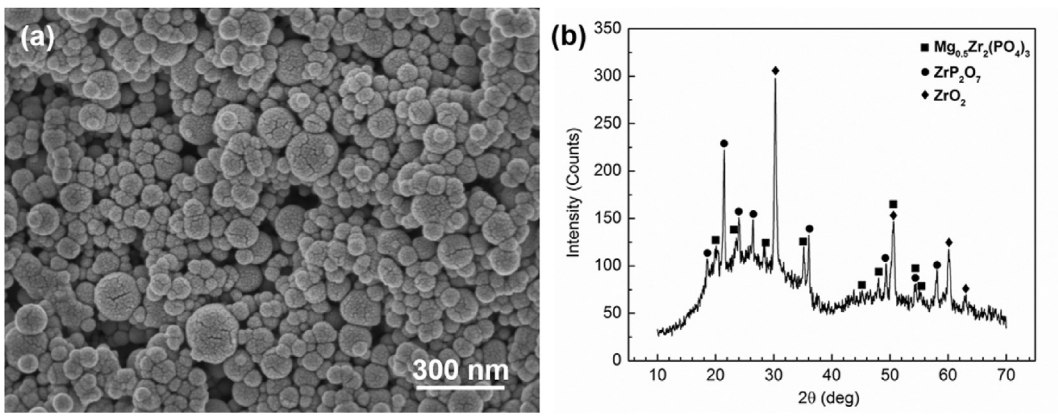

Fig. 1. (a) SEM image and (b) XRD pattern of as-produced $MZPCe_{0.2}$ powders. Note that cracked coating on particle surfaces are sputtered gold added to aid imaging.

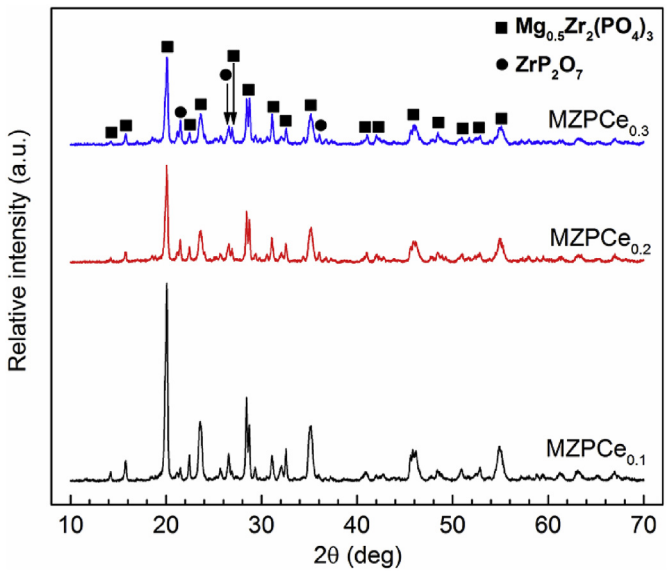

Fig. 2. XRD patterns of $MZPCe_x$ pellets after sintering at 1200 °C/1 h/air.

Optimization of the initial chemical compositions to ensure producing high-purity MZP NPs would be one possible set of studies for future work. Sintering conditions must also be further optimized to produce still higher purity pellet electrolytes.

Lower relative densities and phase purities would lead to lower ionic conductivities of Ce-free MZP, $MZPCe_{0.1}$ and $MZPCe_{0.3}$ pellets. Therefore, only the ionic conductivities of fully dense $MZPCe_{0.2}$ pellets with relative densities of at least 90% were investigated. Fig. 4 provides Nyquist plots in the high frequency regions for $MZPCe_{0.2}$ pellets tested at 100° and 200 °C, respectively. At 100 °C, the Nyquist plot shows a nearly perfect semicircle (<18 MΩ in impedance). An imperfect semicircle at higher frequencies (<0.5 MΩ in impedance) followed by an inclined spike at lower frequencies (>0.5 MΩ in impedance) is observed at 200° vs. 100 °C.

Both plots are typical of ionic conductors with blocking electrodes. The semicircle and spike are due to samples' ionic conductivity and polarization of ion-blocking electrodes [48]. In this study, since the left intercept of the semicircle with the real axis (Z') approaches zero, the right intercept is taken as the total resistance ($R_t = R_g + R_{gb}$) as a conservative estimate: R_g and R_{gb} denote the grain and grain boundary resistances, respectively [37–39]. A well-recognized equivalent circuit, as presented in the inset in Fig. 4a, is used for fitting providing the total resistance. The single resistor (R_1) is equal to the left intercept, the parallel resistor (R_2) to a constant phase element (CPE_1) is equal to the diameter of semicircle, and a constant phase element (CPE_2) denotes electrode polarization [48–51].

Table 3 lists the ionic conductivities of $MZPCe_{0.2}$ pellets tested at 25–200 °C. They offer ionic conductivities of 2.6×10^{-6} mS cm^{-1}at ambient temperature, >10^{-5} mS cm^{-1} at 100 °C, and 3.8×10^{-4} mS cm^{-1} at 200 °C. Relevant discussion is presented in the last section.

3.4. $MZPCe_{0.2}$ films

3.4.1. Sintered film analyses

Per the investigation of $MZPCe_x$ pellet sintering, $MZPCe_{0.2}$ films were sintered at 1000–1200 °C aiming to obtain dense, phase-pure films at temperatures as low as possible.

Fig. 5 XRD patterns reveal phase compositions of the as-sintered $MZPCe_{0.2}$ films. MZP forms in sintered films as well as ZrP_2O_7 as a minor secondary phase. Increasing sintering temperatures and dwell times leads to increases in $Mg_{0.5}Zr_2(PO_4)_3$, and decreases ZrP_2O_7 contents as show in Table 4. High-purity $MZPCe_{0.2}$ films containing >99 wt % MZP were obtained on sintering at 1200 °C/3 h.

Fig. 6 SEMs show fracture morphologies for as-sintered $MZPCe_{0.2}$ films. At 1000 °C, closed-packed spherical NPs are still observed, somewhat similar to as-produced NPs. At 1100 °C, these spherical morphologies disappear accompanied by formation of irregularly-shaped grains. Coincidentally, a large number of pores are distributed uniformly in films. At 1200 °C/1 h, almost no pores can be observed suggesting nearly fully dense films. Longer dwell times (3 h) lead to higher densification and somewhat larger grains. Calculation per Archimedes' method indicates relative densities of 95 ± 2%. The fully dense films (50 μm thick) fracture in an intra-

Table 2
Densities and phase compositions of $MZPCe_x$ pellets after sintering at 1200 °C/1 h/air.

Materials	Density (g cm^{-3})	Relative density (%)	Phases	
			MZP (wt. %)	ZrP_2O_7 (wt. %)
$MZPCe_{0.1}$	2.95	90(±2)	97	3
$MZPCe_{0.2}$	3.32	100(-2)	90	10
$MZPCe_{0.3}$	3.41	100(-2)	87	13

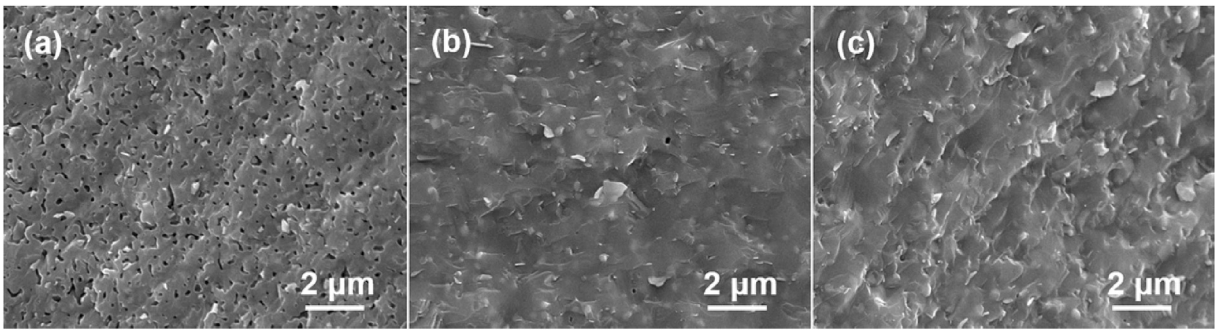

Fig. 3. SEMs of fresh fracture surfaces of (a) $MZPCe_{0.1}$, (b) $MZPCe_{0.2}$ and (c) $MZPCe_{0.3}$ pellets after sintering at 1200 °C/1 h/air.

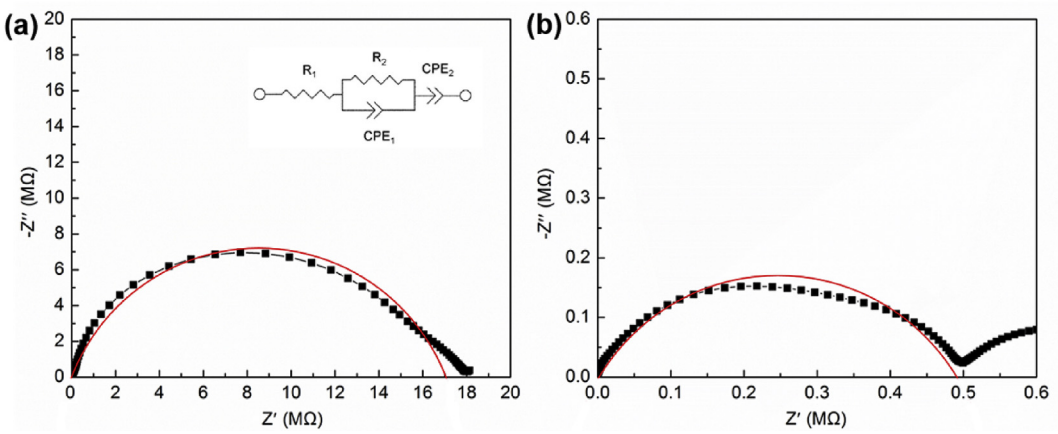

Fig. 4. Representative Nyquist plots for $MZPCe_{0.2}$ pellets tested at (a) 100 °C and (b) 200 °C. The top right insert in (a) is the equivalent circuit used for fitting. R and CPE denote resistors and constant phase elements, respectively.

Table 3
Ionic conductivities of $MZPCe_{0.2}$ pellets after sintering at 1200 °C/1 h/air.

T (C)	25	40	60	80	100	120	140	160	180	200
σ_t ($\times 10^{-5}$ mS cm^{-1})	0.26	0.53	0.63	0.79	1.2	1.9	3.8	8.4	19	38

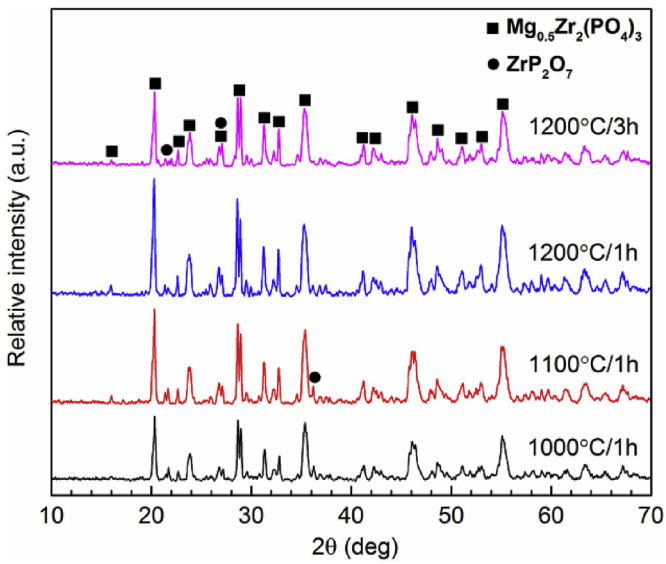

Fig. 5. XRD patterns of $MZPCe_{0.2}$ films after sintering at 1000–1200 °C in air.

Table 4
Relative contents of phases in sintered $MZPCe_{0.2}$films.

Temperature (°C)/Time (h)	MZP (wt. %)	ZrP_2O_7 (wt. %)
1000/1	91.8	8.2
1100/1	93.7	6.3
1200/1	96.1	3.9
1200/3	>99.0	<1.0

granular mode and show a flat fracture surface. Additionally, the white, plate-like grains in Fig. 6c–d correspond to the secondary ZrP_2O_7 phase, as confirmed by TEM, see below.

Initial efforts were made to calculate average grains sizes (AGSs) by observing surface and fracture morphologies of thermally etched $MZPCe_{0.2}$ films using SEM. Both the surfaces and fractured surfaces of the as-sintered films at 1200 °C/3 h were thermally etched at 1100 ± 100 °C/30 min in air. However, only ambiguous grain boundaries or separated grains were observed (SEMs not shown). TEM was then used to investigate AGSs (Fig. S2). Fig. S2a provides a representative TEM of the as-sintered $MZPCe_{0.2}$films at 1200 °C/3 h in air. Grains with clear boundaries were observed. Statistical calculation of dozens of grains based on the lineal intercept method indicates AGSs of 550 ± 100 nm in 45 ± 5 μm thick films. Fig. S2b shows a representative TEM image indicating presence of secondary ZrP_2O_7 phases with AGSs of ca. 200 nm, which is consistent well with the observation of morphologies using SEM (Fig. 6).

Different sintering conditions result in diverse microstructures with variations in phase compositions, grain sizes, phase segregation at grain boundaries and relative densities thereby influencing significantly the ionic conductivity of electrolytes. Low relative densities of electrolytes and purities of the main phase lead to high values for grain boundary resistance [52,53]. A single-phase microstructure with full density and small grain sizes is thus an essential prerequisite for high-performance ionic conductors. Therefore, the ionic conductivities of fully dense $MZPCe_{0.2}$ films with high phase purities (>99%) were investigated as discussed below.

3.4.2. Ionic conductivities

In this work, six $MZPCe_{0.2}$ films sintered at 1200 °C/3 h in air were used to measure ionic conductivities. Conservative results with reproducibility were adopted. Fig. 7 depicts representative Nyquist plots for $MZPCe_{0.2}$ films tested at 100° and 200 °C, respectively. Depressed semicircles at higher frequencies were observed followed by inclined spikes at lower frequencies. The equivalent circuit presented in Fig. 7a inset, as noted in section 3.3, was used for fitting to get the total resistance. The calculated ionic conductivities of $MZPCe_{0.2}$ films measured at 25–280 °C are listed in Table 5. $MZPCe_{0.2}$ films provide conductivities of 1.3×10^{-6} mS cm^{-1} at 60 °C, increasing to 10^{-4} mS cm^{-1} at 200 °C and of 3.1×10^{-3} mS cm^{-1} at 280 °C.

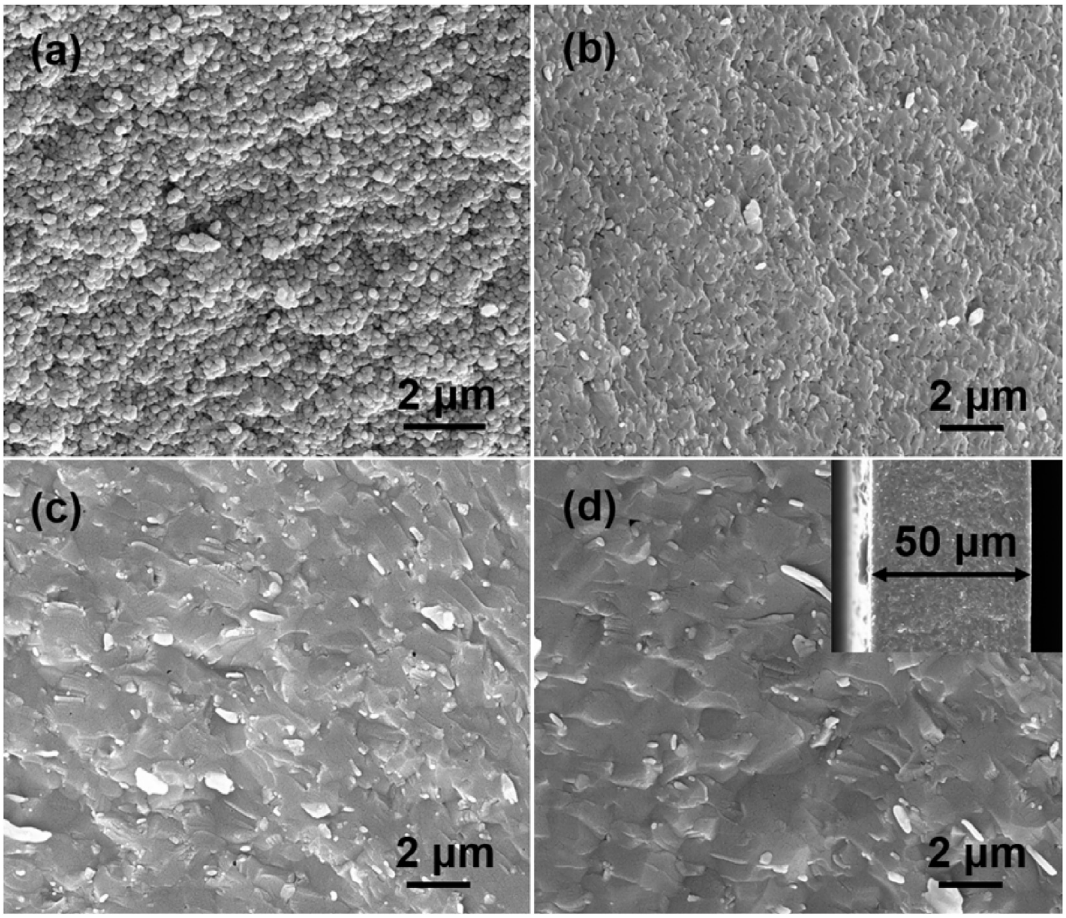

Fig. 6. SEMs of fractured $MZPCe_{0.2}$ films after sintering in air at (a) 1000 °C/1 h, (b) 1100 °C/1 h, (c) 1200 °C/1 h and (d) 1200 °C/3 h.

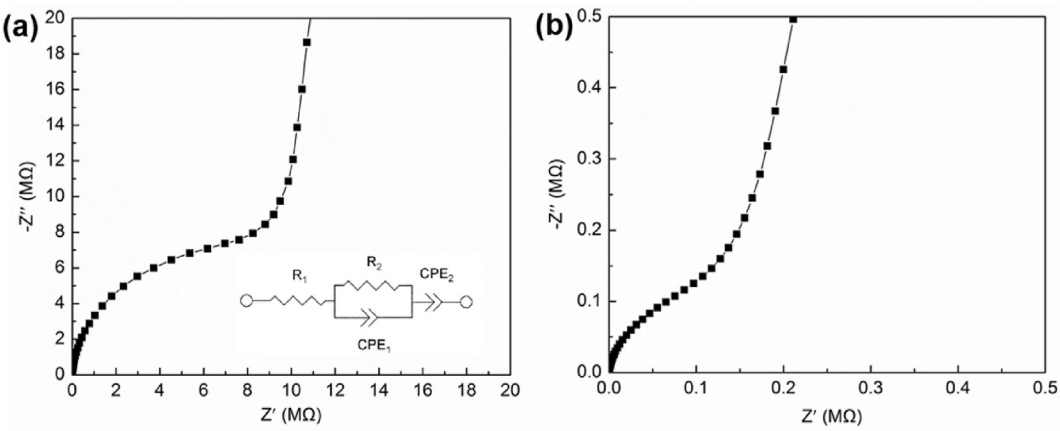

Fig. 7. Representative Nyquist plots for $MZPCe_{0.2}$ film samples tested at (a) 100 °C and (b) 200 °C.The lower right insert in (a) is the equivalent circuit used for fitting, the same as that for pellets in Fig. 5.

Table 5
Total conductivities (σ_t) of $MZPCe_{0.2}$films (43 ± 2 μm thick).

T (°C)	25	40	60	80	100	120	140	160	200	240	280
σ_t ($\times 10^{-5}$ mS cm^{-1})	0.02	0.05	0.13	0.23	0.43	0.81	1.4	3.5	19	91	310

The calculated activation energy is 29.6 kJ/mol (≥60 °C) derived from the slope of Arrhenius plot shown in Fig. 8. Lower activation energies lead theoretically to higher conductivities, while higher activation energies lead to reduced conductivities at lower

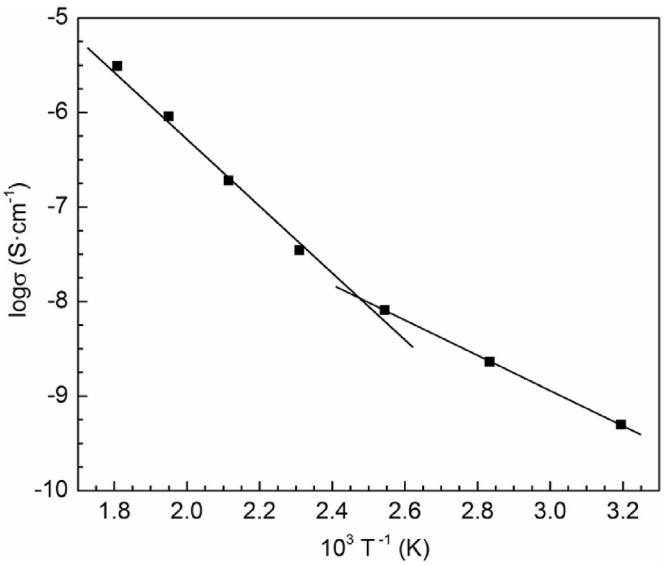

Fig. 8. Arrhenius plot for $MZPCe_{0.2}$ films based on Table 5 data.

Table 6
Estimated conductivities (σ_t) of $MZPCe_{0.2}$ films based on Fig. 8 Arrhenius plot using the extension method.

T (°C)	400	500	600	700	800
σ_t ($\times 10^{-2}$ mS cm^{-1})	4	19	63	166	365

temperatures. As reported elsewhere, $(Mg_{0.1}Hf_{0.9})_{4/3.8}Nb(PO_4)_3$ pellet electrolytes have activation energies of 64 kJ/mol coincident with ionic conductivities of 2.1×10^{-3} mS cm^{-1}at 300 °C [18], 20 times higher than that (1.1×10^{-4} mS cm^{-1}) of $Mg_{0.7}(Zr_{0.85}Nb_{0.15})_4P_6O_{24}$ pellets with higher activation energies of 92 kJ/mol [54].

Per Fig. 8 Arrhenius plot, ionic conductivities of $MZPCe_{0.2}$ films at higher temperatures were estimated by extrapolation, and listed in Table 6. Table 7 compares the ionic conductivities of $MZPCe_{0.2}$ films and pellets to other MZP counterparts reported elsewhere. $MZPCe_{0.2}$ pellets offer conductivities of 3.8×10^{-4} mS cm^{-1} at 20 °C, twice as high as the $MZPCe_{0.2}$ films. The films have relative densities of 95% almost as high as that (98%) of pellets, and phase purities of 99% higher than that (90%) of pellets. The pellet surfaces were polished to obtain a mirror finish before measurement of conductivities. However, the thin films could not be polished easily because they are quite fragile compared to pellets. The low smoothness and even possible surface impurities are likely reasons for the lower conductivities of films vs pellets. The reasonably small AGSs (550 ± 100 nm) of $MZPCe_{0.2}$ films may also lead to lower conductivities.

The $MZPCe_{0.2}$ pellets and thin (≤50 μm) films show conductivities of up to 3×10^{-3} mS/cm^2 at approximately 300 °C in keeping with reported values in the literature. Note that conductivities reported in the open literature to date are only for MZP electrolyte pellets, whereas the present report is the first to produce thin films. Coincidently, films provide lower ionic area specific resistances (IASR = d/σ) due to the significant reduction in thicknesses [35,55–57].

The calculated *IASR for 43 μm $MZPCe_{0.2}$ films was 1400 Ω cm^2 at ≈300 °C*. If we use an E_a of ≈30 kJ/mol then we can extrapolate to suggest that *IASR values for 43 μm $MZPCe_{0.2}$ films would be 110 Ω cm^2 at 400 °C. They are 20$^+$ times smaller than values for 1 mm pellets with almost the same conductivities reported elsewhere* [12,15,18–20]. However, this type of extrapolation can only be verified by actual temperature measurements which are beyond the capability of our current system.

Optimization of Ce-doped MZP NP synthesis, film processing and sintering leading to values of conductivities beyond those reported in open literature remains to be done in future work. MZP electrolytes with new substitutional dopants, e.g. Y^{3+}, are under exploration.

4. Conclusions

$Mg_{0.5}Ce_xZr_{2-x}(PO_4)_3$ (x = 0.1, 0.2 and 0.3) electrolyte NPs were synthesized using liquid-feed flame spray pyrolysis, then processed to pellets (0.5 mm thick) and thin (≤50 μm) films. $Mg_{0.5}Ce_{0.2}Zr_{1.8}(PO_4)_3$ electrolytes including pellets and films after sintering at 1200 °C offer densities and optimized phase purities thereby offering the highest ionic conductivities among the $Mg_{0.5}Ce_xZr_{2-x}(PO_4)_3$ (x = 0.1, 0.2 and 0.3) compositions in this preliminary work. $MZPCe_{0.2}$ pellets show ionic conductivities of 3.8×10^{-4} mS cm^{-1} at 200 °C, while thin (ca. 45 μm thick) films offer values of 1.9×10^{-4} mS cm^{-1} under the same conditions likely due

Table 7
Found and estimated† MZP electrolyte conductivities (σ_t) reported here and elsewhere.

Chemical compositions	T (°C)	σ_t(mS cm^{-1})	Processing methods	Shapes	Refs.
$MZPCe_{0.2}$	25	2.0×10^{-7}	LF-FSP/TC/S	Films/45 ± 5 μm thick	this work
	200	1.9×10^{-4}			
	280	3.1×10^{-3}			
	500†	*1.9×10^{-1}*			
	800†	*3.65*			
$MZPCe_{0.2}$	25	2.6×10^{-6}	LF-FSP/CIP/S	Pellets/0.5 mm thick	this work
	200	3.8×10^{-4}			
$Mg_{0.5}Zr_2(PO_4)_3$	25	1.0×10^{-3}	SG/C/S	Pellets	[15]
	500	7.1×10^{-2}			
$Mg_{0.5}Zr_2(PO_4)_3$	400	2.9×10^{-2}	G/C/HP	Pellets/1–2 mm thick	[29]
	800	6.1×10^{-1}			
$Mg_{0.5}Zr_2(PO_4)_3$	800	6.9×10^{-1}	SG/C/S	Pellets	[17]
$Mg_{1.4}Zr_4P_6O_{24.4}$+$0.4Zr_2O(PO_4)_2$	800	2.9	G/C/S	Pellets	[23]
$Mg_{0.9}(Zr_{0.6}Fe_{0.4})_2(PO_4)_3$	25	1.3×10^{-2}	SG/C/S	Pellets	[16]
	500	7.2×10^{-2}			
$Mg_{0.5}Si_2(PO_4)_3$	25	1.8×10^{-2}	SG/C/S	Pellets	[27]
$(Mg_{0.1}Hf_{0.9})_{4/3.8}Nb(PO_4)_3$	300	2.1×10^{-3}	CP/C/S	Pellets	[18]

Note: TC—tape casting, S-sintering at atmospheric pressure, CIP—cold isostatic pressing, SG—sol-gel, C—calcination, G—grinding mixed powders in a mortar, HP—hot pressing, CP—co-precipitation.

to the imperfect surface finishes and possible surface impurities. Note that Ce free compositions do not sinter to full density under the conditions used here indicating the advantage to doping with Ce.

Arrhenius based estimates for ionic conductivities at 400 °C suggest values near or superior to 10^{-2} mS cm^{-1} in keeping with the best values reported in the literature. The important contribution here is the significant reduction in thickness in these thin film electrolytes compared to pellets which offer IASR values of 1400 Ω cm^2 at ≈ 300 °C and are estimated to offer IASR values of 110 Ω cm^2 at 400 °C providing the potential for high energy density solid-state batteries. Thin film electrolytes are therefore promising for development of high-performance all-solid-state Mg-ion batteries operated at medium temperatures.

The optimization of the electrolyte composition, microstructure, and processing conditions is underway which is expected to achieve maximum ionic conductivities to open a new door for the applications of rechargeable batteries. Substantial research efforts will be made to develop competitive magnesium electrolytes by processing of thin films with new chemical compositions.

The results reported here suggest that it may be possible to greatly improve the Mg^{2+} conductivities in dense, thin ceramic electrolytes to the point where the operational temperatures of solid state batteries made from them will function at temperatures below 200 °C and perhaps eventually below 100 °C, as we have successfully shown recently for dense, flexible Li^+ ceramic electrolytes [37–39].

Conflicts of interest

There are no conflicts to declare.

Acknowledgements

We are grateful for the financial support of this work by NSF through DMR-1105361 and 116058. BL, as an international exchange visitor, would also like to thank the support from Harbin Institute of Technology. RML and BY thank the support of China 111 Project (Grant No. B16032) for exchange between laboratories. Finally RML would like to acknowledge a gift of funds from Daimler AG that was used in partial support of the work reported here.

Appendix A. Supplementary data

Supplementary data related to this article can be found at https://doi.org/10.1016/j.electacta.2018.04.015.

References

[1] L. Baggetto, R.A.H. Niessen, F. Roozeboom, P.H.L. Notten, High energy density all-solid-state batteries: a challenging concept towards 3D integration, Adv. Funct. Mater. 18 (2008) 1057–1066.
[2] M. Ogawa, K. Yoshida, K. Harada, All-solid-state lithium batteries with wide operating temperature range, SEI Tech. Rev. 74 (2012) 89.
[3] F. Du, N. Zhao, Y. Li, C. Chen, Z. Liu, X. Guo, All solid state lithium batteries based on lamellar garnet-type ceramic electrolytes, J. Power Sources 300 (2015) 24–28.
[4] A. Hooper, B.C. Tofield, All-solid-state batteries, J. Power Sources 11 (1984) 33–41.
[5] H. Kitaura, H. Zhou, All-solid-state lithium-oxygen battery with high safety in wide ambient temperature range, Sci. Rep. 5 (2015) 13271.
[6] M.M. Huie, D.C. Bock, E.S. Takeuchi, A.C. Marschilok, K.J. Takeuchi, Cathode materials for magnesium and magnesium-ion based batteries, Coord. Chem. Rev. 287 (2015) 15–27.
[7] P. Novak, R. Imhof, O. Haas, Magnesium insertion electrodes for rechargeable nonaqueous batteries—a competitive alternative to lithium? Electrochim. Acta 45 (1999) 351–367.
[8] H.D. Yoo, I. Shterenberg, Y. Gofer, G. Gershinsky, N. Pour, D. Aurbach, Mg rechargeable batteries: an on-going challenge, Energy Environ. Sci. 6 (2013) 2265.
[9] P. Saha, M.K. Datta, O.I. Velikokhatnyi, A. Manivannan, D. Alman, P.N. Kumta, Rechargeable magnesium battery: current status and key challenges for the future, Prog. Mater. Sci. 66 (2014) 1–86.
[10] D. Aurback, Y. Gofer, Z. Lu, A. Schechter, O. Chusid, H. Gizbar, Y. Cohen, V. Ashkenazi, M. Moshkovich, R. Turgeman, E. Levi, A short review on the comparison between Li battery systems and rechargeable magnesium battery technology, J. Power Sources 97–98 (2001) 28–32.
[11] H.D. Yoo, Y. Liang, Y. Li, Y. Yao, High areal capacity hybrid magnesium-lithium-ion battery with 99.9% coulombic efficiency for large-scale energy storage, ACS Appl. Mater. Interfaces 7 (2015) 7001–7007.
[12] N. Wu, Z.-Z. Yang, H.-R. Yao, Y.-X. Yin, L. Gu, Y.-G. Guo, Improving the electrochemical performance of the $Li_4Ti_5O_{12}$ electrode in a rechargeable magnesium battery by lithium–magnesium Co-Intercalation, Angew. Chem. Int. Ed. 54 (2015) 5757–5761.
[13] R. Mohtadi, M. Matsui, T.S. Arthur, S.-J. Hwang, Magnesium borohydride: from hydrogen storage to magnesium battery, Angew. Chem. 124 (2012) 9918–9921.
[14] P. Canepa, S.-H. Bo, G. S.Gautam, B. Key, W. D. Richards, T. Shi, Y. Tian, Y. Wang, J. Lia, G. Cedera, "High magnesium mobility in ternary spinel chalcogenides," Nat. Commun.. DOI: 10.1038/s41467-017-01772-1.
[15] N.K. Anuar, S. Adnan, N.S. Mohamed, Characterization of $Mg_{0.5}Zr_2(PO_4)_3$ for potential use as electrolyte in solid state magnesium batteries, Ceram. Int. 40 (2014) 13719–13727.
[16] N.K. Anuar, S.B.R.S. Adnan, M.H. Jaafar, N.S. Mohamed, Studies on structural and electrical properties of $Mg_{0.5+y}(Zr_{2-y}Fe_y)_2(PO_4)_3$ ceramic electrolytes, Ionics 22 (2016) 1125–1133.
[17] M. Adamu, G.M. Kale, Novel sol-gel synthesis of $MgZr_4P_6O_{24}$ composite solid electrolyte and newer insight into the Mg^{2+}-ion conducting properties using impedance spectroscopy, J. Phys. Chem. C 120 (2016) 17909–17915.
[18] S. Tamura, M. Yamane, Y. Hoshino, N. Imanaka, Highly conducting divalent Mg^{2+} cation solid electrolytes with well-ordered three-dimensional network structure, J. Solid State Chem. 235 (2016) 7–11.
[19] A. Omote, S. Yotsuhashi, Y. Zenitani, Y. Yamada, High ion conductivity in $MgHf(WO_4)_3$ solids with ordered structure: 1-D alignments of Mg^{2+} and Hf^{4+} ions, J. Am. Ceram. Soc. 94 (2011) 2285–2288.
[20] K. Nomura, S. Ikeda, K. Ito, H. Einaga, Ionic conduction behavior in zirconium phosphate framework, Solid State Ionics 61 (1993) 293–301.
[21] S. Ikeda, M. Takahashi, J. Ishikawa, K. Ito, Solid electrolytes with multivalent cation conduction. 1. Conducting species in Mg-Zr-PO4 system, Solid State Ionics 23 (1987) 125–129.
[22] S. Ikeda, S. Kato, K. Nomura, K. Ito, H. Einaga, S. Saito, Y. Fujita, Carbon dioxide sensor using solid electrolytes with zirconium phosphate framework, Solid State Ionics 70 (1994) 569–571.
[23] N. Imanaka, Y. Okazaki, G. Adachi, Divalent magnesium ion conducting characteristics in phosphate based solid electrolyte composites, J. Mater. Chem. 10 (2000) 1431–1435.
[24] G.M. Kale, K.T. Jacob, L. Wang, Y. Hong, Solid-state electrochemical sensor for monitoring Mg in Al refining process, Electrochem. Soc. Trans. 1 (2005) 1–11.
[25] L. Wang, R.V. Kumar, A new SO_2 gas sensor based on an Mg^{2+} conducting solid electrolyte, J. Electroanal. Chem. 543 (2003) 109–114.
[26] S. Ikeda, T. Kondo, S. Kato, K. Ito, K. Nomura, Y. Fujita, Carbon dioxide sensor using solid electrolytes with zirconium phosphate framework (2). Properties of the CO2 gas sensor using Mg1.15Zr4P5.7Si0.3O24 as electrolyte, Solid State Ionics 79 (1995) 354–357.
[27] Z.A. Halima, S.B.R.S. Adnan, N.S. Mohamed, Effect of sintering temperature on the structural, electrical and electrochemical properties of novel $Mg_{0.5}Si_2(PO_4)_3$ ceramic electrolytes, Ceram. Int. 42 (2016) 4452–4461.
[28] S. Hui, J. Roller, S. Yick, X. Zhang, C. Deces-Petit, Y. Xie, R. Maric, D. Ghosh, A brief review of the ionic conductivity enhancement for selected oxide electrolytes, J. Power Sources 172 (2007) 493–502.
[29] K. Nomura, S. Ikeda, K. Ito, H. Einaga, Substitution effect of framework constituents on electrical property of solid electrolytes with β-$Fe_2(SO_4)_3$-type structure, $M_{1+x}Zr_2P_{3-x}SixO_{12}$ (M=Li, 1/2 Mg, and 1/2 Zn), Chem. Lett. 21 (1992) 1897–1900.
[30] R. Zhao, J. Liu, J. Gu, The effects of electrode thickness on the electrochemical and thermal characteristics of lithium ion battery, Appl. Energy 139 (2015) 220–229.
[31] F. Jiang, P. Peng, Elucidating the performance limitations of lithium-ion batteries due to species and charge transport through five characteristic parameters, Sci. Rep. 6 (2016) 32639.
[32] H. Zheng, J. Li, X. Song, G. Liu, S. Battaglia, A comprehensive understanding of electrode thickness effects on the electrochemical performances of Li-ion battery cathodes, Electrochim. Acta 71 (2012) 258–265.
[33] J. Choi, B. Son, M.-H. Ryou, S.H. Kim, J.M. Ko, Y.M. Lee, Effect of LiCoO2 cathode density and thickness on electrochemical performance of Lithium-ion batteries, J. Electrochem. Sci. Technol 4 (2013) 27–33.
[34] P.G. Balakrishnan, R. Ramesh, T. Prem Kumar, Safety mechanisms in lithium-ion batteries, J. Power Sources 155 (2006) 401–414.
[35] C. Ma, E. Rangasamy, C. Liang, J. Sakamoto, K.L. More, M. Chi, Excellent stability of a lithium-ion-conducting solid electrolyte upon reversible Li^+/H^+ exchange in aqueous solutions, Angew. Chem. Int. Ed. 54 (2015) 129–133.
[36] B.D. McCloskey, Attainable gravimetric and volumetric energy density of Li-S and Li-ion battery cells with solid separator protected Li metal anodes, J. Phys. Chem. Lett. 6 (2015) 4581–4588.
[37] E. Yi, W. Wang, S. Mohanty, J. Kieffer, R. Tamaki, R.M. Laine, Materials that can

replace liquid electrolytes in Li batteries: superionic conductivities in $Li_{1.7}Al_{0.3}Ti_{1.7}Si_{0.4}P_{2.6}O_{12}$. Processing combustion synthesized nanopowders to free standing thin films, J. Power Sources 269 (2014) 577–588.
[38] E. Yi, W. Wang, J. Kieffer, R.M. Laine, Flame made nanoparticles permit processing of dense, flexible, Li^+ conducting ceramic electrolyte thin films of cubic-$Li_7La_3Zr_2O_{12}$ (c-LLZO), J. Mater. Chem. A 4 (2016) 12947–12954.
[39] E. Yi, W. Wang, J. Kieffer, R.M. Laine, Key parameters governing the densification of cubic-$Li_7La_3Zr_2O_{12}$ Li^+ conductors, J. Power Sources 352 (2017) 156–164.
[40] T.R. Hinklin, J. Azurdia, M. Kim, J.C. Marchal, S. Kumar, R.M. Laine, Finding spinel in all the wrong places, Adv. Mater. 20 (2008) 1373–1375.
[41] R.M. Laine, J. Marchal, H.J. Sun, X.Q. Pan, A new $Y_3Al_5Oi_2$ phase produced by liquid-feed flame spray pyrolysis (LF-FSP), Adv. Mater. 17 (2005) 830–833.
[42] C.R. Bickmore, K.F. Waldner, R. Baranwal, T. Hinklin, D.R. Treadwell, R.M. Laine, Ultrafine titania by flame spray pyrolysis of a titanatrane complex, J. Eur. Ceram. Soc. 18 (1998) 287–297.
[43] C.R. Bickmore, K.F. Waldner, D.R. Treadwell, R.M. Laine, Ultrafine spinel powders by flame spray pyrolysis of a magnesium aluminum double alkoxide, J. Am. Ceram. Soc. 79 (1996) 1419–1423.
[44] J.A. Azurdia, J. Marchal, P. Shea, H. Sun, X.Q. Pan, R.M. Laine, Liquid-feed flame spray pyrolysis as a method of producing mixed-metal oxide nanopowders of potential interest as catalytic materials. Nanopowders along the NiO-Al_2O_3 tie line including $(NiO)_{0.22}(Al_2O_3)_{0.78}$, a new spinel composition, Chem. Mater. 18 (2006) 731–739.
[45] A.S. Bondarenko, G.A. Ragoisha, in: A.L. Pomerantsev (Ed.), Progress in Chemometrics Research, Nova Science Publishers, New York, 2005, pp. 89–102 the program is available online at: http://www.abc.chemistry.bsu.by/vi/analyser/.
[46] S.B.R.S. Adnan, N.S. Mohamed, Characterization of novel $Li_4Zr_{0.06}Si_{0.94}O_4$ and $Li_{3.94}Cr_{0.02}Zr_{0.06}Si_{0.94}O_4$ ceramic electrolytes for lithium cells, Ceram. Int. 40 (2014), 6473–6379.
[47] S.B.R.S. Adnan, N.S. Mohamed, Properties of novel $Li_{4-3x}Cr_xSiO_4$ ceramic electrolyte, Ceram. Int. 40 (2014) 5033–5038.
[48] P.G. Bruce, A.R. West, The A-C conductivity of polycrystalline LISICON, $Li_{2+2x}Zn_{1-x}GeO_4$, and a model for intergranular constriction resistances, J. Electrochem. Soc. 130 (1983) 662–669.
[49] H.S. Jadhav, M.-S. Cho, R.S. Kalubarme, J.-S. Lee, K.-N. Jung, K.-H. Shin, C.-J. Park, Influence of B_2O_3 addition on the ionic conductivity of $Li_{1.5}Al_{0.5}Ge_{1.5}(PO_4)_3$ glass ceramics, J. Power Sources 241 (2013) 502–508.
[50] N. Imanishi, S. Hasegawa, T. Zhang, A. Hirano, Y. Takeda, O. Yamamoto, Lithium anode for lithium-air secondary batteries, J. Power Sources 185 (2008) 1392–1397.
[51] M.A. Wang, X.L. Feng, Y.C. Zhao, S.J. Li, G.J. Geng, H. Xia, Y.H. Lin, C.W. Nan, Enhanced ionic transport in lithium lanthanum titanium oxide solid state electrolyte by introducing silica, Solid State Ionics 179 (2008) 2255–2259.
[52] S. Hui, J. Roller, S. Yick, X. Zhang, C. Deces-Petit, Y. Xie, R. Maric, D. Ghosh, A brief review of the ionic conductivity enhancement for selected oxide electrolytes, J. Power Sources 172 (2007) 493–502.
[53] H. Aono, E. Sugimoto, Y. Sadaoka, N. Imanaka, G. Adachi, Ionic conductivity of solid electrolytes based on lithium titanium phosphate, J. Electrochem. Soc. 137 (1990) 1023–1027.
[54] N. Imanaka, Y. Okazaki, G. Adachi, Divalent magnesium ionic conduction in $Mg_{1-2x}(Zr_{1-x}Nb_x)_4P_6O_{24}$ (x=0-0.4) solid solution, Electrochem. Solid state Lett. 3 (2000) 327–329.
[55] E.D. Wachsman, K.T. Lee, Lowering the temperature of solid oxide fuel cells, Science 334 (2011) 935–939.
[56] V. Dusastre, J.A. Kilner, Optimization of composite cathodes for intermediate temperature SOFC applications, Solid State Ionics 126 (1999) 163–174.
[57] K. Huang, P.Y. Hou, J.B. Goodenough, Reduced area specific resistance for iron-based metallic interconnects by surface oxide coatings, Mater. Res. Bull. 36 (2001) 81–95.